Weighted Ensemble Transform Kalman Filter for Image Assimilation

Sébastien Beyou, Anne Cuzol, Sai Subrahmanyam Gorthi, Etienne Mémin

Tellus **000**, 000–000 (0000) Printed November 12, 2012 (Tellus LaTeX style file v2.2)

Weighted Ensemble Transform Kalman Filter for Image Assimilation

By Sebastien Beyou, Anne Cuzol, Sai Subrahmanyam Gorthi and Etienne Mémin ⋆ ,

INRIA, campus de Beaulieu, 35042 Rennes Cedex, France

November 12, 2012

ABSTRACT

This paper proposes an extension of the Weighted Ensemble Kalman filter (WEnKF) proposed by Papadakis et al. (2010) for the assimilation of image observations. The main contribution of this paper consists in a novel formulation of the Weighted filter with the Ensemble Transform Kalman filter (WETKF) incorporating directly as a measurement model a nonlinear image reconstruction criterion. This technique has been compared to the original WEnKF on numerical and real world data of 2D turbulence observed through the transport of a passive scalar. It has been in particular applied for the reconstruction of oceanic surface current vorticity fields from Sea Surface Temperature satellite data. This latter technique enables a consistent recovery of oceanic surface currents, vorticity maps along time in presence of large missing data areas and strong noise.

1 Introduction

The analysis of geophysical fluid flows is of crucial interest in Oceanography, Meteorology, or Hydrology for forecasting applications, or for the monitoring of hazards. In all those domains a great number of orbital or geostationary satellites provides a huge amount of image data with still increasing spatial and temporal resolutions. The combination of such fine scale observations with larger scales dynamical models in data assimilation schemes might be of great interest to infer with a greater accuracy the evolution of the observed geophysical fluid flows. Compared to *in situ* measurement techniques supplied by dedicated

⋆ Correspondingauthor.

e-mail: etienne.memin@inria.fr

probes or Lagrangian drifters, satellite images give access to a much denser observation field but provide unfortunately only an indirect access to the physical quantities of interest. The direct estimation from a satellite image sequence of the flow state variables leads hence to difficult inverse problems. This is particularly true for the recovery of fluid flow motion fields from successive pairs of images. Such a direct estimation is intrinsically ill-posed and requires the introduction of additional smoothing constraints imposed either globally on the image domain in variational approaches (see Heitz et al. (2010) for a review) or within a local window in correlation based techniques (Adrian, 1991; Emery et al., 1986; Ottenbacher et al., 1997; Szantai et al., 2002). Those techniques rely heavily on this implicit or explicit smoothing assumption and are prone to strong errors in presence of noise, missing data or regions of low photometric variability. Consequently, there is a strong difficulty in imposing a trajectorial consistency to the sequence of (generally independently) estimated motion fields. In the best scenario case these methods provide accurate instantaneous displacements only for a limited range of scales and experience severe difficulties for medium to small scales measurements due to the smoothing prior used. Their accuracy is also restricted to regions that exhibit sufficient luminance variations. Although these techniques are very useful to measure in a fast and tireless way motion fields from an image sequence, all these difficulties generate in large areas inconsistent measurements along time in real world atmospheric or oceanic satellite images.

One way to enforce such a dynamical consistency of the velocity measurements consists in embedding the estimation problem within an image based assimilation process. Variational assimilation of image information has been recently considered by several authors for the tracking along time of convective cells (Thomas et al., 2010) or for the estimation of consistent motion fields (Corpetti et al., 2009; Titaud et al., 2010; Papadakis and Mémin, 2008). All these techniques have been assessed on simplified dynamics: level set transport equation associated to a transportation component defined from motion measurements with Brownian uncertainties for Thomas et al. (2010), different forms of the Shallow-water equations for Corpetti et al. (2009) and Titaud et al. (2010) or 2D velocity-vorticity Navier-Stokes formulation in Papadakis and Mémin (2008). The techniques differ mainly in the way they are dealing with the relation linking the measurements and the state variables (the observation operator). In Corpetti et al. (2009); Thomas et al. (2010) linear observation operators derived from the normal equations associated to a local least square motion estimation formulation are considered. The problem is addressed in a slightly different way in Titaud

et al. (2010), simulating from an initial image a sequence transported by the state variable dynamics. The observation operator is then defined as a relation between this simulated sequence and the observed image sequence. This approach relies on the hypothesis that the actual image sequence is close to a reference sequence transported by the model.

Let us note that all these techniques may incorporate either preconditioning stages in their internal iterative optimization or covariance specifications that include smoothing functional similar as those employed for the motion estimation problems (Souopgui et al., 2009).

Another family of data assimilation procedures is defined as stochastic filters implemented through Monte Carlo samples called ensemble members or particles whether the filtering is implemented through an ensemble Kalman filter or with a particle filter. Contrary to the previous deterministic techniques, those assimilation schemes aim at recovering a description of the probability density function of the state variable trajectory based on the complete history of measurements up to the current instant. These schemes have the advantage to deal with the whole nonlinearity of the dynamics and to include directly a representation of the uncertainty associated to the considered dynamics. Obviously the building of such a stochastic model is debatable on the precise form it may take. However, this ability is very interesting in cases for which the dynamical model is only imprecisely known. Let us note that second order variational methods allows also computing the error covariance matrix through second order adjoint systems (Le Dimet et al., 2002). This is however at the price of a significant computational cost increase.

Recently a data assimilation procedure embedding an Ensemble Kalman filter into the particle filter framework, entitled Weighted Ensemble Kalman filter, has been proposed (Papadakis et al., 2010). This filter combines all the nice properties of the ensemble Kalman mechanics with the correction scheme of the particle filter. Conceptually, this filter is more adapted to a non Gaussian distribution of the ensemble members, which is a situation that may arise at very short time horizon with nonlinear stochastic dynamics [1]. It has been also shown experimentally that this modified filter exhibits a faster convergence. This has been however assessed only on synthetic 2D turbulence models in the simple case of measurements artificially built from a noisy version of the true simulated data (Papadakis et al., 2010). The main contribution of the paper consists thus first in extending the study of WEnKF

[1] Other solutions have been proposed to deal with non-Gaussianity in the framework of variational methods or stochastic filters (interested readers may refer to the review of Bocquet et al. (2010) or Yang et al. (2012))

to the assimilation of observations supplied by image data. We will mainly focus on the incorporation of a direct image reconstruction error measurement. Here the great advantage is to avoid the use of external techniques to supply so called pseudo observations at the price of a nonlinear observation operator. The second purpose of the paper lies in extending the weighted ensemble framework based on randomly sampling of the measurement noise (referred usually as ensemble schemes with perturbed observation (Evensen, 1994; Houtekamer and Mitchell, 1998) to a weighted version that uses the ensemble transform Kalman filter (ETKF), proposed by Bishop et al. (2001) and developed by Tippett et al. (2003) and Wang et al. (2004). This transform is built from a (mean-preserving) square-root matrix to update the mean and covariances, in accordance with the Kalman update equations. This extension was suggested in Papadakis et al. (2010) but was not implemented. We will see that this transform is well adapted to the case of nonlinear direct image measurements and enables processing the fluid flow image sequences directly, without the need of any intermediate velocity fields observations. The proposed WETKF makes use of the ETKF mechanism as the proposal distribution of the particle filter and corrects the different members according to the particle filtering selection step. This selection scheme associates to each ensemble member a filtering weight determined in our case through a mean square error of displaced frame differences, and performs a resampling favoring particles corresponding to high values of the filtering probability distribution.

We organize the paper as follows: Section 2 recalls the principles governing the construction of the Weighted Ensemble Kalman filter proposed in Papadakis et al. (2010). After a brief discussion of ensemble transform Kalman filter in Section 2.2, we describe its particle filter extension. Its application to fluid flow analysis through the direct observation of an image sequence depicting the transportation of a passive scalar is presented in Section 3. Section 4 presents the experimental validation of these approaches and brings out some elements of comparison. Real results on 2D sequences of 2D turbulence and satellite oceanic data are presented. Finally, Section 5 concludes the paper with a discussion to future directions.

2 Assimilation with the weighted ensemble transform Kalman filter

We describe in this section how the assimilation problem can be formulated sequentially by a filtering approach adapted to a nonlinear and high-dimensional framework.

2.1 Filtering in a nonlinear and high-dimensional setting

Stochastic filters aim at estimating the posterior probability distribution $p(\mathbf{x}_{0:k}|\mathbf{y}_{1:k})$ of a state variable trajectory $\mathbf{x}_{0:k}$ starting from an initial state $\mathbf{x}_0$ up to the state $\mathbf{x}_k \in \mathbb{R}^n$ at current time k. The state variable trajectory is obtained through the integration of a dynamical system:

$$\mathrm{d}\mathbf{x}_t = \mathbf{M}(\mathbf{x}_t)\mathrm{d}t + \boldsymbol{\eta}\mathrm{d}\mathbf{B}_t, \tag{1}$$

where $\mathbf{M}$ denotes a deterministic linear/nonlinear dynamical operator, corresponding to a physical conservation law describing the state evolution. The random part $\mathrm{d}\mathbf{B}_t$ accounts for the uncertainties in the deterministic state model. It is usually a Gaussian noise, white in time but correlated in space with covariance $\mathbf{Q} = \boldsymbol{\eta}\boldsymbol{\eta}^T$. It is assumed that the true state is unknown and observed through $\mathbf{y}_k \in \mathbb{R}^m$ at discrete time instants. These observations are assumed to be linked to the state variable through the following measurement equation:

$$\mathbf{y}_k = \mathbf{H}(\mathbf{x}_k) + \boldsymbol{\gamma}_k, \tag{2}$$

where the observation noise $\boldsymbol{\gamma}_k$ is a white Gaussian noise with covariance matrix $\mathbf{R}$ and $\mathbf{H}$ stands for the linear/nonlinear mapping from the state variable space to the observation space. We note that the (integration) time step used for the state variable dynamics δt is usually much smaller (about 10-100 times), than the time interval δk between two subsequent measurements. A sequence of measurements or observations from time 1 to k will be denoted by a set of vectors of dimension m as: $\mathbf{y}_{1:k} = \{\mathbf{y}_i, i = 1, \ldots, k\}$, where the time between two successive measurements is arbitrarily set to $\delta k = 1$.

In a nonlinear context, it is known that the filtering equations can no longer be solved by the Kalman algorithm and its direct variants. Ensemble Kalman filters (Anderson and Anderson, 1999; Bishop et al., 2001; Evensen, 1994; Houtekamer and Mitchell, 1998; Ott et al., 2004) have been developed to tackle the filtering problem in nonlinear and high-dimensional systems. However, these methods still rely on a Gaussian assumption. On the other hand, particle filters (Doucet et al., 2000; Del Moral, 2004; Gordon et al., 1993) are able to solve exactly the filtering equations (up to the Monte Carlo approximation). But, in their simplest formulation, they are not suitable to high-dimensional systems (van Leeuwen, 2009; Snyder et al., 2008).

Particle filtering techniques implement an approximation of the state posterior density

$p(\mathbf{x}_{0:k}|\mathbf{y}_{1:k})$ (called filtering law), using a sum of N weighted Diracs:

$$p(\mathbf{x}_{0:k}|\mathbf{y}_{1:k}) \approx \sum_{i=1}^{N} w_k^{(i)} \delta_{\mathbf{x}_{0:k}^{(i)}}(\mathbf{x}_{0:k}), \tag{3}$$

centered on hypothesized elements (called particles) of the state space sampled from a proposal distribution $\pi(\mathbf{x}_{0:k}|\mathbf{y}_{1:k})$. This distribution, called the importance distribution, approximates the true filtering distribution. Each sample is then weighted by a weight, $w_k^{(i)}$, accounting for the ratio between the two distributions. Any importance function can be chosen (with the only restriction that its support contains the filtering distribution one). Under weak hypotheses the importance ratio can be recursively defined as:

$$w_k^{(i)} \propto w_{k-1}^{(i)} \frac{p(\mathbf{y}_k|\mathbf{x}_k^{(i)}) p(\mathbf{x}_k^{(i)}|\mathbf{x}_{k-1}^{(i)})}{\pi(\mathbf{x}_k^{(i)}|\mathbf{x}_{0:k-1}^{(i)}, \mathbf{y}_{1:k})}. \tag{4}$$

By propagating the particles $\{\mathbf{x}_k^{(i)}, i = 1, \ldots, N\}$ from time $k-1$ through the proposal density $\pi(\mathbf{x}_k|\mathbf{x}_{0:k-1}^{(i)}, \mathbf{y}_{1:k})$, and by weighting the sampled states with $w_k^{(i)}$, a recursive sampling of the filtering law is obtained. The standard choice when applying the particle filter is to fix the proposal distribution to the transition law $p(\mathbf{x}_k|\mathbf{x}_{k-1})$. In that case, it is easy to sample from the proposal (this requires only to sample from the dynamical model (1)). However, this choice has the major drawback of sampling the particles without taking into account the observation $\mathbf{y}_k$. This makes the particle filter not suitable in a high-dimensional context. As a matter of fact, particles are led to explore the state space blindly following the dynamical model only and are most of the time far away from the observation at correction time, yielding hence very quickly to a filter divergence. It is thus necessary to introduce the observation within the proposal distribution in order to guide the particles, and then make the particle filtering technique suitable to high-dimensional problems (van Leeuwen, 2009). Such a strategy has been used in Papadakis et al. (2010) through the ensemble Kalman filter mechanism. Relying on the usual assumption of the ensemble techniques (*i.e.* considering the dynamics as a discrete Gaussian system), the proposal can be set to a Gaussian conditional distribution $\pi(\mathbf{x}_k|\mathbf{x}_{k-1}^{(i)}, \mathbf{y}_k)$. In order to make the estimation of the filtering distribution exact (up to the sampling), each member of the ensemble must be weighted at each instant k, with appropriate weights $w_k^{(i)}$ defined from (4). With a systematic resampling scheme and for high dimensional systems represented on the basis of a very small number of ensemble members it can be shown (Papadakis et al., 2010) that the weights reduces to the computation of the data likelihood:

$$w_k^{(i)} \propto p(\mathbf{y}_k|\mathbf{x}_k^{(i)}), \tag{5}$$

with $\sum_{i=1}^{N} w_k^{(i)} = 1$. Those weights may be thus interpreted through (3) as the *a posteriori* probability associated to the sample trajectory $\mathbf{x}_k^{(i)}$ and provide for the filtering objective a natural quality ranking of a given sample. In the following we describe how this ensemble Kalman proposal step can be performed with a particular scheme called the Ensemble Transform Kalman Filter.

2.2 Ensemble transform Kalman filter

Several forms of ensemble Kalman filters have been successfully proposed since the seminal work of Evensen (Evensen, 1994). Those filters which correspond to the ensemble or particle implementation of the Kalman Filter (Kalman, 1960) have demonstrated their performances in geophysical sciences as they allow propagating very high-dimensional state vectors. This advantage springs from the ability of the EnKF to approximate or compute the forecast and analysis two first moments (needed in KF recursion) directly from the ensemble, while propagating the ensemble members through the exact dynamics and observation models, without an explicit linearization – as it is done in Extended Kalman filter (Anderson and Moore, 1979). The EnKF avoids explicit computation of the covariance matrix, which may not even be affordable in very high-dimensional states, and further the algorithms of Evensen (2003) or Bishop et al. (2001) present computationally efficient schemes for the inversion of the covariance matrix required in the Kalman gain computation, through a low dimensional singular value decomposition, when the number of ensemble members is much lower than the state dimension, which is usually the case.

Two kinds of ensemble filters have been proposed so far in the literature. The first kind of method (Evensen, 2003) introduces artificially perturbed observations in order to enable a complete Monte Carlo estimation of the mean and covariance of the filtering distribution. This technique has been reported to yield good Gaussian approximation in a nonlinear regime but may show some bias for a too small ensemble. The second kind of techniques relies on so-called deterministic square-root filters. Among the different variations of square-root filters, the Ensemble Transform Kalman filters, proposed by Bishop et al. (2001) and developed by Tippett et al. (2003) and Wang et al. (2004), employ a (mean-preserving) square-root matrix to update the mean and covariances, in accordance with the Kalman update equations. We present now the essential ideas of this scheme.

Considering first a linear observation operator $\mathbf{H}$, the covariance and mean update equa-

tions in the Kalman filter at instant k are respectively given by:

$$\mathbf{P}_k^a = \mathbf{P}_k^f - \mathbf{P}_k^f \mathbf{H}^T (\mathbf{H}\mathbf{P}_k^f \mathbf{H}^T + \mathbf{R})^{-1} \mathbf{H}\mathbf{P}_k^f, \tag{6}$$

$$\bar{\mathbf{x}}_k^a = \bar{\mathbf{x}}_k^f + \mathbf{P}_k^a \mathbf{H}^T \mathbf{R}^{-1} (\mathbf{y}_k - \mathbf{H}\bar{\mathbf{x}}_k^f), \tag{7}$$

where superscript "f" stands for the forecast step, whereas "a" corresponds to the correction step (also called analysis) and the overline symbol denotes the empirical average. Using a forecasted ensemble members perturbation centered around the mean, $\mathbf{X}_k^f = \{\mathbf{x}_k^{f,(i)} - \bar{\mathbf{x}}_k^f, i = 1, \ldots, N\}$, an empirical approximation of the forecast covariance is obtained as: $\mathbf{P}_k^f = (N-1)^{-1} \mathbf{X}_k^f \mathbf{X}_k^{f^T}$, and we get:

$$(N-1)\mathbf{P}_k^a = \mathbf{X}_k^f \mathbf{X}_k^{f^T} - \mathbf{X}_k^f \mathbf{X}_k^{f^T} \mathbf{H}^T (\mathbf{H}\mathbf{X}_k^f \mathbf{X}_k^{f^T} \mathbf{H}^T + \tilde{\mathbf{R}})^{-1} \mathbf{H}\mathbf{X}_k^f \mathbf{X}_k^{f^T},$$

with $\tilde{\mathbf{R}} = (N-1)\mathbf{R}$. Let us note that in general the ensemble dimension N is much lower than the state space dimension ($N << n$). A nonlinear observation operator $\mathbf{H}(\mathbf{X}_k^f)$, can be incorporated by replacing $\mathbf{H}\mathbf{X}_k^f$ with a centered matrix $\mathbf{H}(\mathbf{X}_k^f)$, defined as:

$$\mathbf{H}(\mathbf{X}_k^f) = \{\mathbf{H}(\mathbf{x}_k^{f,(i)}) - \overline{\mathbf{H}(\mathbf{x}_k^f)}, i = 1, \ldots, N\}. \tag{8}$$

The same expression of the nonlinear observation is used in Houtekamer and Mitchell (2001); Hunt et al. (2007). This leads to the following approximate covariance update with a nonlinear observation model:

$$(N-1)\mathbf{P}_k^a = \mathbf{X}_k^f \mathbf{X}_k^{f^T} - \mathbf{X}_k^f \mathbf{H}(\mathbf{X}_k^f)^T (\mathbf{H}(\mathbf{X}_k^f)\mathbf{H}(\mathbf{X}_k^f)^T + \tilde{\mathbf{R}})^{-1} \mathbf{H}(\mathbf{X}_k^f) \mathbf{X}_k^{f^T},$$

which can be written under the form $(N-1)\mathbf{P}_k^a = \mathbf{X}_k^f \mathbf{D}_k \mathbf{X}_k^{f^T}$ with:

$$\mathbf{D}_k = \mathbf{I} - \mathbf{H}(\mathbf{X}_k^f)^T (\mathbf{H}(\mathbf{X}_k^f)\mathbf{H}(\mathbf{X}_k^f)^T + \tilde{\mathbf{R}})^{-1} \mathbf{H}(\mathbf{X}_k^f), \tag{9}$$

and where $\mathbf{I}$ is the $N \times N$ identity matrix. Writing $(N-1)\mathbf{P}_k^a = \mathbf{X}_k^a \mathbf{X}_k^{a^T}$ where $\mathbf{X}_k^a$ gathers desired centered corrected ensemble members, and expressing $\mathbf{D}_k = \mathbf{A}_k \mathbf{A}_k^T$ through its matrix square root, we get $\mathbf{X}_k^a \mathbf{X}_k^{a^T} = \mathbf{X}_k^f \mathbf{A}_k \mathbf{A}_k^T \mathbf{X}_k^{f^T}$, or $\mathbf{X}_k^a = \mathbf{X}_k^f \mathbf{A}_k$. In order to compute the matrix square-root $\mathbf{A}_k$, we rely on the Sherman-Morison-Woodbury formula as suggested by Tippett et al. (2003) and which leads to:

$$\mathbf{D}_k = (\mathbf{I} + \mathbf{H}(\mathbf{X}_k^f)^T \tilde{\mathbf{R}}^{-1} \mathbf{H}(\mathbf{X}_k^f))^{-1}. \tag{10}$$

From the eigenvalue decomposition:

$$\mathbf{I} + \mathbf{H}(\mathbf{X}_k^f)^T \tilde{\mathbf{R}}^{-1} \mathbf{H}(\mathbf{X}_k^f) = \mathbf{U}_k (\mathbf{I} + \mathbf{\Lambda}_k) \mathbf{U}_k^T, \tag{11}$$

where $\mathbf{U}_k$ is an orthogonal matrix the square root $\mathbf{A}_k$ can be written as:

$$\mathbf{A}_k = \mathbf{U}_k (\mathbf{I} + \mathbf{\Lambda}_k)^{-1/2}. \tag{12}$$

Note however that this square-root is not unique and can be replaced by $\mathbf{A}_k \mathbf{V}$, where $\mathbf{V}$ is

any arbitrary orthonormal matrix ($\mathbf{V}\mathbf{V}^T = \mathbf{I}$) of suitable dimension. In particular, one can look for a mean preserving square-root such that:

$$\mathbf{X}_k^a \mathbf{1} = \mathbf{X}_k^f \mathbf{A}_k \mathbf{1} = 0, \tag{13}$$

where $\mathbf{1}$ is a vector of ones. As the forecast ensemble is centered by definition, this condition is fulfilled for an ensemble matrix $\mathbf{X}_k^f$ of rank $N-1$ if and only if $\mathbf{A}_k\mathbf{1} = \alpha\mathbf{1}$. It can be shown (Ott et al., 2004; Sakov and Oke, 2007; Wang et al., 2004) , that taking:

$$\mathbf{A}_k = \mathbf{U}_k(\mathbf{I} + \mathbf{\Lambda}_k)^{-1/2}\mathbf{U}_k^T. \tag{14}$$

satisfies the above mean preserving condition for the transform. The improvement brought by the use of this mean preserving transform over non mean preserving square root filters or ensemble filters with perturbed observations has been experimentally shown and analyzed in Sakov and Oke (2007).

As a final step a mean analysis term $\bar{\mathbf{x}}_k^a$ has to be added to each element $\mathbf{x}_k^{a,(i)}$. The mean analysis vector reads:

$$\bar{\mathbf{x}}_k^a = \bar{\mathbf{x}}_k^f + (N-1)^{-1}\mathbf{X}_k^f \mathbf{D}_k \mathbf{H}(\mathbf{X}_k^f)^T \mathbf{R}^{-1}(\mathbf{y}_k - \mathbf{H}(\bar{\mathbf{x}}_k^f)). \tag{15}$$

Note that computing (10) only requires the inversion of a $N \times N$ matrix, if the inverse of the measurement error covariance matrix $\mathbf{R}$ is available. Usually $\mathbf{R}$ is defined as a diagonal or band diagonal (very sparse) matrix and is easy to invert. The analysis step can thus be accomplished efficiently. In our case $\mathbf{R}$ will be assumed to be a diagonal matrix and is thus trivially inverted. Let us note that in the case of image data, it would be very interresting to investigate the use of sparse banded information matrices ($\mathbf{R}^{-1}$) associated to statistical graphical models (Lauritzen, 1996).

Ensemble filters may be also accompanied with so-called localization procedures introduced to discard spurious long range correlations that appear in empirical covariance matrices built from a small number of samples. Such a localization procedure is carried out either explicitely by considering only the observation within a window centered around a given point grid, or implicitely by introducing in the forecast covariance matrix a factor decaying gradually to zero as the distance between two grid points increases.

2.3 Weighted ensemble transform Kalman filter

We describe here how to perform the assimilation of observation $\mathbf{y}_k$ at time k, *i.e.* how to update sequentially the filtering distribution from $\hat{p}(\mathbf{x}_{k-1}|\mathbf{y}_{1:k-1}) = \sum_{i=1}^N w_{k-1}^{(i)} \delta_{\mathbf{x}_{k-1}^{(i)}}(\mathbf{x}_{k-1})$

to $p(\mathbf{x}_k|\mathbf{y}_{1:k}) = \sum_{i=1}^{N} w_k^{(i)} \delta_{\mathbf{x}_k^{(i)}}(\mathbf{x}_k)$. The extension to the ensemble transform Kalman filter (ETKF) of the WEnKF described in Papadakis et al. (2010) is straightforward. It consists in sampling the ensemble members from the ETKF procedure and then to weight these members according to their likelihood (5). A final resampling is then performed, drawing a new set of N members from the ensemble with probabilities proportional to their weights. Those steps are summarized below.

At time k, starting from a set of N particles $\{\mathbf{x}_{k-1}^{(i)}, i = 1, \ldots, N\}$, one iteration of the WETKF algorithm splits into the following steps:

- Get $\mathbf{x}_k^{a,(i)}$ from the forecast and analysis steps of ETKF:
  - *Forecast*: For all $i = 1, \ldots, N$, simulate $\mathbf{x}_k^{f,(i)}$ from model (1), with initial condition $\mathbf{x}_{k-1}^{a,(i)}$ and a given discrete scheme with time step δt;
  - *Analysis*: Compute $\mathbf{x}_k^{a,(i)}$ from Section 2.2.
- Compute particle filter weights $w_k^{(i)} \propto p(\mathbf{y}_k|\mathbf{x}_k^{a,(i)})$.
- Resample particles to obtain $\{\mathbf{x}_k^{(i)}, i = 1, \ldots, N\}$ and set $w_k^{(i)} = \frac{1}{N}$ for all $i = 1, \ldots, N$.

Let us note that the final resampling step is implemented with a small Gaussian perturbation of the ensemble members. This random perturbation avoids a strict duplication of some members and implements an additive inflation procedure as it is usually done in ensemble Kalman filtering implementation. There is no particular constraint on the proposal ETKF step, it may thus includes any additional localization or inflation procedure. This extension could be for instance applied to localized ETKF version Hunt et al. (2007); Ott et al. (2004).

3 Fluid motion estimation from images

In this section, we describe the application of the proposed WETKF method to the problem of fluid motion estimation from a sequence of images.

3.1 Dynamical model

In this work we will rely on the 2D vorticity-velocity formulation of the Navier-Stokes equation with a stochastic forcing to encode the dynamics uncertainty terms. Let $\xi(\boldsymbol{x})$ denote the scalar vorticity at point $\boldsymbol{x} = (x, y)^T$, associated to the 2D velocity $w(\boldsymbol{x}) = (w_x(\boldsymbol{x}), w_y(\boldsymbol{x}))^T$ through $\xi(\boldsymbol{x}) = \frac{\partial w_y}{\partial x} - \frac{\partial w_x}{\partial y}$. Let $\boldsymbol{\xi} \in \mathbb{R}^{|\Omega_\xi|}$ be the state vector describing the vorticity over a spatial domain Ω_ξ of size $|\Omega_\xi|$, and $\mathbf{w} \in \mathbb{R}^{2|\Omega_\xi|}$ the associated velocity field

over the same domain. For incompressible flows, the stochastic dynamics is then written:

$$\mathrm{d}\boldsymbol{\xi}_t = -\nabla\boldsymbol{\xi}_t \cdot \mathbf{w}\mathrm{d}t + \nu\Delta\boldsymbol{\xi}_t\mathrm{d}t + \eta\mathrm{d}\mathbf{B}_t \tag{16}$$

where ν is the viscosity coefficient and $\mathrm{d}\mathbf{B}_t$ is random forcing term. This a white in time noise model is an isotropic homogeneous random field corresponding to idealistic turbulence toy model (Kraichnan, 1968; Majda and Kramer, 1999). It is characterized spatially by a covariance model $\mathbf{Q}$ exhibiting a power-law function spatial within an inertial range of scale. These random fields are in practice simulated in the Fourier domain (Elliot et al., 1997; Evensen, 2003).

Note that the velocity field can be recovered from its vorticity, for incompressible fluids, using the Biot-Savart integral as: $\mathbf{w} = \nabla^{\perp}G \star \boldsymbol{\xi}$, where $G(.) = \frac{\ln(|.|)}{2\pi}$ is the Green kernel associated to Laplacian operator and $\nabla^{\perp} = (-\partial_y, \partial_x)^T$ represents the orthogonal gradiant. This transformation can be efficiently implemented in Fourier domain, noting that $\Delta\Psi = \boldsymbol{\xi}$ and $\mathbf{w} = \nabla^{\perp}\Psi$, where Ψ represents the stream function.

3.2 Nonlinear image observation model

There are two ways to assimilate the image data within the system. The first solution consists in computing pseudo-observations (motion estimates) from two consecutive images. This leads to a linear observation model. Another approach consists in observing directly the image data, which makes the problem harder since the observed quantity is then a highly nonlinear function of the system state. As shown in the previous section, such a nonlinearity in the observation model can be handled within the WETKF framework.

In order to assimilate directly the image data, a nonlinear image observation model that relies on the brightness consistency assumption can be formulated as follows:

$$I(\boldsymbol{x}, k) = I(\boldsymbol{x}_{k+1}, k+1) + \gamma_k(\boldsymbol{x}) \quad \forall \boldsymbol{x} \in \Omega_I, \tag{17}$$

where I is the luminance function, Ω_I is the spatial image domain, $\boldsymbol{x}_{k+1} = \boldsymbol{x} + \mathbf{d}(\boldsymbol{x})$ is the displaced point at time $k+1$ and $\mathbf{d}(\boldsymbol{x}) = \int_k^{k+1} \mathbf{w}(\boldsymbol{x}_t)dt$ denotes the displacement between time k and time $k+1$, with the initial point location at time k fixed to the grid point $\boldsymbol{x}$ (i.e. $\boldsymbol{x}_k = \boldsymbol{x}$).

Let $\mathbf{I}_k$ be the vector gathering values $I(\boldsymbol{x}, k)$ for all $\boldsymbol{x}$ in the image domain Ω_I. This vector constitutes the observation at time k. It is nonlinearly related to the state vector $\boldsymbol{\xi}_k$ through the luminance function of the image data at time $k+1$. The perturbation γ_k

is a Gaussian random field with covariance $\mathbf{R}$. This measurement noise is assumed to be independent of the dynamics noise.

In the following, since this nonlinear image model will be used within the WETKF framework, the covariance $\mathbf{R}$ will be assumed to be diagonal in order to compute the analysis step more efficiently (see section 2.2). The uncertainty $\gamma_k(\boldsymbol{x})$ is then a Gaussian random variable of variance $\mathbf{R}(\boldsymbol{x},\boldsymbol{x}) = \sigma_k^2(\boldsymbol{x})$. As the displaced image difference depends on the unknown displacement, this variance depends necessarily on the state variable (which is not contradictory with the independence property between the noise dynamics and the measurement noise). We propose to estimate empirically the variance from the ensemble members:

$$\sigma_k^2(\boldsymbol{x}) = \frac{1}{N-1}\sum_{i=1}^{N}(I(\boldsymbol{x}+\mathbf{d}^{(i)}(\boldsymbol{x}),k+1) - \overline{I_d}(\boldsymbol{x},k+1))^2 + \epsilon, \tag{18}$$

where $\overline{I_d}$ denotes the empirical mean of the displaced image. The parameter ϵ corresponds to a minimal variance value associated to homogeneous photometric regions. Let us note that in order to enforce some homogeneity between neighbor perturbations, a small Gaussian smoothing is applied to this variance.

The likelihood of observations (used to compute the particles weights) is then written:

$$p(\mathbf{I}_k|\boldsymbol{\xi}_k^{(i)}) \propto \exp\left(-\sum_{\boldsymbol{x}=1}^{|\Omega|}\frac{\left(I(\mathbf{x},k) - I(\boldsymbol{x}+\mathbf{d}^{(i)}(\boldsymbol{x}),k+1)\right)^2}{\mathbf{R}(\boldsymbol{x},\boldsymbol{x})}\right). \tag{19}$$

3.3 Image assimilation scheme

We summarize in this section the WETKF image assimilation technique for fluid flow estimation.

At time $k=0$, the vorticity $\hat{\boldsymbol{\xi}}_0$ is initialized from a given motion estimator applied on the two first images $\mathbf{I}_0$ and $\mathbf{I}_1$.

For $k = 1,\ldots,K$, the following steps are performed to estimate $\hat{\boldsymbol{\xi}}_k$:

- Obtain $\{\boldsymbol{\xi}_k^{(i)}, i=1,\ldots,N\}$ and associated weights $w_k^{(i)}, i=1,\ldots,N$ from the WETKF algorithm described in section 2.3, with the following practical details:

  – In order to compute the forecast step, estimated vorticity maps $\{\boldsymbol{\xi}_{k-1}^{(i)}, i=1,\ldots,N\}$ at previous step have to be propagated from the dynamical model (16). This supplies the forecast ensemble members $\boldsymbol{\xi}_k^{f,(i)}$, at time k, as the Itô integral:

$$\boldsymbol{\xi}_k^{f,(i)} = \boldsymbol{\xi}_{k-1}^{(i)} + \int_{k-1}^{k}(\nu\Delta\boldsymbol{\xi}_t^{f,(i)} - \nabla\boldsymbol{\xi}_t^{f,(i)}\cdot\mathbf{w}(\boldsymbol{\xi}_t^{f,(i)}))\mathrm{d}t + \eta\int_{k-1}^{k}\mathrm{d}\mathbf{B}_t, \tag{20}$$

where the velocity $\mathbf{w}(\boldsymbol{\xi}_t^{f,(i)})$ is recovered from the Biot-Savart integral (see Section 3.1). In practice, equation (20) is discretized with the Euler-Maruyama method (Kloeden and Platen, 1999) associated to a small time increment δt. A conservative numerical scheme (Shu, 1998) is used for the advective term $\nabla\xi \cdot \mathbf{w}$, which respects the (flux) conservation law by integrating the flux values at cell boundaries. This total variation diminishing (TVD) scheme (monotonically preserving flux) prevent from an increase in oscillations over time and enable to transport shocks, as detailed in Shu (1998). The Laplacian is implemented through a centered finite difference scheme.

– The analysis step of ETKF is performed with observation model (17), where the image data $\mathbf{I}_k = \{I(\boldsymbol{x}, k) \quad \forall \boldsymbol{x} \in \Omega_I\}$ constitutes the observation at time k, nonlinearly related to the vorticity state vector.

– Weights are computed from the likelihood (19).

– The variance of observation noise defined by (18) is not valid in missing data areas. Such regions appear frequently in oceanic data due to the cloud cover (see the experiments on oceanic data in Section 4.3) or correspond to areas occluded by layers of higher altitudes than the layer of interest in meteorological images. The absence of measurement can in general be easily identified. For such regions we propose to impose a high uncertainty. The idea here is to rely either on dynamics or on the neighborhood estimates rather than on false interpolated measurements. The strength of these uncertainties is set to a value proportional to the number of missing data over a centered local window. The magnitude of the proportionality factor is scaled to the highest uncertainty of the data (excluding the missing data). Moreover, for coastal regions, a mask corresponding to the land region is created with zero velocity values (Dirichlet boundary conditions). The dynamical update and measurement correction are frozen on such locations.

• Compute the vorticity estimate $\hat{\boldsymbol{\xi}}_k$ as the weighted average $\hat{\boldsymbol{\xi}}_k = \sum_{i=1}^{N} w_k^{(i)} \boldsymbol{\xi}_k^{(i)}$, and associated mean velocity fields estimates $\hat{\mathbf{w}}_k$ through Biot-Savart integration.

4 Experimental results

In this section, the proposed image assimilation method will be tested on synthetic and real sequences describing nonlinear and high-dimensional fluid phenomena. Results will be compared to another data assimilation method which can be used within this framework: the weighted ensemble Kalman filter (WEnKF, Papadakis et al. (2010)) which also relies on

an ensemble Kalman filtering step, integrated within a particle filtering framework. In Papadakis et al. (2010), the WEnKF was used to assimilate linear observations. In case of image data that is nonlinearly related to the state of the system, these linear observations consist in pseudo-observations, *i.e.* velocity fields (and associated vorticity maps) computed from a given motion estimation technique. In the experiments below, these pseudo-observations are computed from a stochastic version of the well-known Lucas and Kanade motion estimator (Corpetti and Mémin, 2012), applied on each pair of the image sequence.

Let $\tilde{\mathbf{w}}_k$ be the velocity field estimated by the stochastic Lucas-Kanade method, called SLK in the following, and $\tilde{\boldsymbol{\xi}}_k$ its corresponding vorticity. The observation model is written than as:

$$\tilde{\boldsymbol{\xi}}_k(\boldsymbol{x}) = \boldsymbol{\xi}_k(\boldsymbol{x}) + \gamma_k(\boldsymbol{x}), \tag{21}$$

with $\gamma_k(\boldsymbol{x}) = \sigma_k(\boldsymbol{x})\eta_k(\boldsymbol{x})$ where η_k is a Gaussian random field with given covariance $g_\lambda(\boldsymbol{x}-\boldsymbol{y})$, and $\sigma_k(\boldsymbol{x})$ is defined by the uncertainties of the motion measurements at each point $\mathbf{x}$ (obtained as an output of the SLK method). The additive uncertainty γ_k is then a Gaussian random field with non-stationary variance $\mathbf{R}(\boldsymbol{x},\boldsymbol{x}) = \sigma_k^2(\boldsymbol{x})$, and covariance $\mathbf{R}(\boldsymbol{x},\boldsymbol{y}) = \sigma_k(\boldsymbol{x})\sigma_k(\boldsymbol{y})g_\lambda(\boldsymbol{x}-\boldsymbol{y})$.

The likelihood of observations (used to compute the particle weights) reads then:

$$p(\tilde{\boldsymbol{\xi}}_k|\boldsymbol{\xi}_k^{(i)}) \propto \exp\left(-\frac{1}{2}(\tilde{\boldsymbol{\xi}}_k - \boldsymbol{\xi}_k^{(i)})^T\mathbf{R}^{-1}(\tilde{\boldsymbol{\xi}}_k - \boldsymbol{\xi}_k^{(i)})\right). \tag{22}$$

As noted in Papadakis et al. (2010), a singular value decomposition of the $|\Omega_I| \times N$ observation perturbations matrix can be performed in order to compute efficiently this likelihood.

4.1 Results on a synthetic 2D image sequence

Our first set of experiments concerns a synthetic image sequence with images of size 256×256 showing the transport of a passive scalar by a forced 2D turbulent flow. This sequence is, to some extent, representative of typical satellite images depicting transport processes by oceanic streams, such as sea surface temperature or sea color images. This scalar exhibits a small diffusion, and does not respect strictly a luminance conservation assumption. Furthermore, due to low spatial gradients of this scalar in large areas (see Fig. 3-(a)), most of the usual motion estimators perform quite poorly on this sequence. The parameters of the power law function involved in the model noise covariance are here fixed from the ground truth data. The noise samples have thus in this case the same energy spectrum as the reference. The model noise standard deviation has been set to 0.01 for all the

experiments. For the nonlinear image measurement model, the observation noise covariance has been first fixed to a constant diagonal matrix with a unity standard deviation. Some trials with an image dependant observation covariance are shown at the end of this section. Let us outline that the vorticity dynamics used for the filtering does not corresponds here exactly to a perfect dynamical model as the true deterministic forcing of the 2D turbulence is unknown and represented only by a zero mean random field.

The results are first compared in terms of global RMSE between the ground truth vorticity and the estimated vorticity at each time step, and similarly for the motion fields. The WEnKF and WETKF results have been obtained with $N = 700$ particles. As may be observed on Figure 1, the improvement obtained with the WEnKF filtering technique over SLK measurements is minor, and even deteriorates the results in terms of velocity fields reconstruction. The proposed WETKF technique, directly based on image luminance observations, leads to much better results for the estimation of vorticity and velocity fields.

In addition to global error comparisons, the analysis of spectra allows to observe more precisely the accuracy of the different techniques at different scales. As a matter of fact the RMSE constitutes only a performance measure at large scales. It is indeed interesting to note that all methods give relatively coherent results only from the large scales up to the beginning of the inertial range. On the other hand, the result obtained with the WETKF assimilation scheme is closer to the ground truth over the whole scale range (from the largest scales up to the small dissipative scales). Again, this comes from the fact that this technique can take benefit of all available information in the image data, while pseudo-observations given by a local motion estimator will not be able to improve the estimation at all scales. Filters based on pseudo-observations are unable to correct the loss of energy caused by the smoothing operator used in the external estimation procedure.

For a qualitative visual comparison, estimated vorticity maps are plotted on Figure 3 at a given time instant. The scalar image observation is first presented, together with the ground truth vorticity on Figure 3(b). Figure 3(c) shows the vorticity estimated with the local SLK technique. The result obtained with the WEnKF assimilation scheme based on these SLK observations is presented on Figure 3(d), while Figure 3(e) shows the result obtained with the proposed WETKF technique, assimilating image data directly. As can be seen on Figure 3(c), the vorticity estimated by the local motion estimation technique is far from the ground truth. As a consequence, the WEnKF assimilation based on these measurements only brings a small improvement since these observations do not carry enough information. The solution

clearly lacks of energy compared to the true vorticity. The direct assimilation of image data through the WETKF scheme leads to a better estimation of vorticity structures, and in particular of small scales structures as discussed previously with the comparison of spectra.

To conclude, note that the improvement obtained with the WETKF technique comes not only from the direct introduction of image data within the assimilation system, but also from the chosen ETKF strategy for the ensemble Kalman step. We highlight this improvement on Figure 4, comparing the image assimilation technique with the ETKF scheme and standard EnKF scheme where the linear observation operator $\mathbf{H}\mathbf{x}_k$ is replaced by $\mathbf{H}(\mathbf{x}_k)$ as described in section 2.2 equ. (8) for the ETKF approach. Figure 4 shows that the best results are obtained with the ETKF scheme, for different sample sizes.

On this benchmark, we also compared in terms of vorticity the results obtained by WETKF and a similar ETKF version (non weighted implementation of the filter). The results corresponding to different amounts of ensemble members are gathered in tables 6 (a-b). These results correspond to the average mean square error obtained over the last 20 images of the sequence and 10 realizations. The first table shows the root mean square vorticity error associated to the empiral mean, whereas the second table gives the mean square dispersion of the ensemble around the ground truth (*i.e.* $(N-1)^{-1}\sum_i \|\boldsymbol{\xi}_k^{a,(i)} - \boldsymbol{\xi}_{ref}\|^2$). It can be observed that the results for ETKF and WETKF remain of the same order. The first moment and the ensemble dispersion are sligtly lower for the weighted version. It is however important to outline that RMSE constitutes only a large scale criterion. To draw finer conclusions it is interesting to observe the error power spectrum (spectrum of the difference between the reference and the results averaged on the last 20 images and 10 realizations). These curves are plotted in figure 5(a) in log-$k\times$spectrum for different number of particles. This graph depicts the amount of energy of the velocity error ($\mathbf{w}_{err} = \mathbf{w} - \mathbf{w}_{ref}$) for each frequency band. For comparison purpose the ground truth spectrum and these curves are reproduced in the inside box graph. The error energy curves obtained by ETKF are plotted in dotted lines whereas those corresponding to WETKF are in plain line. It can be noticed that for both methods and for the different number of particles the error energy is mainly concentrated within a frequency band corresponding to 80 to 8 pixels and the error energy bump inside this range decreases significantly when the number of particles increases. The results obtained with 10 particles have much higher error energy than for the other amount of particles and are not acceptable. There is clearly a limit number of particles below which errors are too important. For 50 particles WETKF provides lower errors on almost all the

whole frequency range that concentrates the most part of the energy. Another point of view can be obtained from error power spectrum in log-log scale normalized by the ground truth power spectrum. This is shown in figure 5(b). As can be observed for 10 particles there is no scale range for which the normalized error energy drops below 10%. For 50 particles this 10% error limit scale corresponds to 40 pixels. For 400 particles this scale reaches 25 pixels. Hence for both methods, low energy error levels are only obtained at coarse scales and accurate results at fine resolution requires to significantly augment the particles. For a weak number of particles WETKF seems to perform slighly better than ETKF whereas for a higher number of particles both filter provides very similar results.

The figure 8 depicts the spatial maps of the second order moment. For both methods the evolution of this moment is plotted. We can observe that WETKF provides in a faster way a smoother variance map and ETKF shows at some localized places a higher variance. The ensemble covariance values for the center line is also pictured (for 50 ensemble members) for WETKF and ETKF. Both techniques provide comparable results in terms of covariance length scale (around 15 pixels).

As a last result on this sequence, we plot in figure 7 an example of the image-based observation variance (18). It is interesting to see that high variance value concentrates on thin structures corresponding to high photometric gradients. For this observation covariance and 400 particles we plot the evolution of the root mean square error. We notice this parameter free covariance observation model yields a better result than the previous constant variance.

The results described in this section comfort us on the use of the WETKF. The weight updating step and the resampling are not computationally expensive and strengthen the robustness of ensemble Kalman filter for relative low number of particles. In the following we will rely uniquely on such filters.

4.2 Results on real 2D turbulence

The next set of experiments corresponds to real experimental images of a passive scalar transported by a turbulent flow. This image sequence corresponds to the experiments described in Jullien et al. (2000). The size of images is 512×512, and WEnKF and WETKF results have been obtained with $N = 300$ particles. Vorticity results at a given time instant are plotted on Figure 9 for the SLK technique, and both WEnKF (assimilating SLK results) and WETKF (assimilating image data). We note that the SLK motion estimation

technique captures only coarse-scale vortices. The scales are successfully refined with the WEnKF assimilation relying on the same measurement and with the WETKF assimilation incorporating directly the nonlinear image reconstruction error. The WETKF image assimilation reveals small motion scales exhibiting vortex filaments or stretching areas, which are smoothed out by SLK and WEnKF methods. This can be observed in particular inside the white delimited area of Figure 9(d-e-f), zoomed in on Figure 9(g-h-i). It must be pointed out that for the three techniques the estimated motion fields are quite close at large scale, so the results are consistent although based on different measurement operators. This might help validating these results, even if the ground truth is unknown here.

4.3 Results on oceanic data

Our final set of results concerns the application of the proposed WETKF technique on satellite images of Sea Surface Temperature (SST), with large areas of missing data due to the cloud cover and presence of coastal regions.

First of all, in order to highlight the capability of the method to cope with missing data, it is tested on a synthetic oceanic sequence. This sequence has been built from an initial real world 200×200 SST image transported by a synthetic flow, and respects the brightness consistency assumption given by (17). The synthetic flow is the same 2D turbulent flow as the one used in section 4.1. Along the whole sequence, four square holes with side 20-45 pixels have been added randomly on each image. Figure 10 shows an example at a given time k of the sequence. Figures 10(a) and 10(b) show two consecutive images of the sequence, with the corresponding simulated ground truth velocity and vorticity on Figure 10(c). The result obtained with the WETKF assimilation scheme is presented on Figure 10(d) from the images without missing data, and on Figure 10(e) for the images with holes. It can be observed that the vorticity and velocity fields are estimated accurately, even in the presence of missing data. As a matter of fact, since for such regions the method relies on the dynamical model or on neighborhood estimates, the spatiotemporal consistency is maintained. The results can be compared on Figure 6 in terms of global RMSE between the mean estimates and the ground truth at each time step. The accuracy of the estimation deteriorates in presence of missing data, but the error level remains low and stable with time.

The method is then tested on a real oceanic sequence of SST images. The sequence consists of 48 images of size 256×256. The images have a spatial resolution of 0.1 degree (10

km) and a temporal period of 24 hours. The sequence is centered on an area of the Pacific ocean off the Panama isthmus and shot during an El Niño episode. Representative results at different time instants of the sequence are shown in Figure 12. The first column of Figure 12 shows the estimated velocity fields at times $k = 1, 10, 24$ and $k = 39$, superimposed on the corresponding SST images. The second column shows the estimated vorticity maps and velocity fields. The initialization for image 1 is based on the estimation provided by the local motion estimation approach (SLK). We see that this initialization provides only a rough large scale motion field. This estimate is refined afterward by the filtering process. We can note that the motion fields estimated along the sequence stick quite well to the big image structures observed on the SST images. The sequence of motion fields does not seem to be perturbed by the big missing data regions observed intermittently. Finally, we can note that the result obtained shows well an increase of the turbulent agitation with an intensification of the El-Niño phenomenon.

Let us note there seems to be a good adequation between the 2D vorticity dynamics used here and the data model based on (local in time) conservation of the observed quantity (the SST). This coupling enables extracting a 2D component explaining the image observation deformation and which is consistent with a 2D flow. The incorporation of more realistic 3D oceanic models would require more advanced data model allowing explaining luminance variations in a consistent way with respect to the dynamical models. In that prospect, the elaboration of data models relying on physical conservation laws might be of interest (Heitz et al., 2010).

5 Conclusion and discussion

In the context of image data assimilation, this paper extends to mean preserving square root filters (Wang et al., 2004) the weighted ensemble strategy proposed in Papadakis et al. (2010). This technique is defined as a particle filter in which the state variable trajectories sampling mechanism (*i.e.* the proposal distribution) is defined from an ensemble Kalman filter. This type of proposal function revealed to be experimentally much more efficient than the traditional sequential importance sampling based on the dynamics alone. Furthermore compared to an importance sampling based on perturbed observations, a mean preserving square root filter sampling has shown to be more efficient for high-dimensional state space and a highly nonlinear observation equation. A significant improvement was brought by

this nonlinear observation over velocity and uncertainty measurements provided by a local motion estimation techniques (Corpetti and Mémin, 2012). Pseudo-observation of flow velocities constructed from local motion estimator techniques such as the Lucas and Kanade estimator (Lucas and Kanade, 1981) corresponds to measurements at too coarse scales. These measurements should not be used in image based data assimilation. As those estimators have generally better performances than correlation techniques on scalar images (such as top of cloud pressure, sea surface temperature, sea color, etc.) the same conclusion applies also to maximum cross correlation or particle image velocimetry techniques. The nonlinear reconstruction error based on the displaced frame difference criterion has demonstrated to provide much better results. This criterion relies on a noisy transport assumption from frame to frame. This transport assumption is however only local since it applies only on the time interval in between two images. It is thus a weaker assumption than a strong transport assumption over the whole assimilation window used in Titaud et al. (2010). Besides it enables when coupled with ensemble techniques to access to empirical observation error covariance that can easily be adapted to missing information regions. This ability has allowed us to apply such an assimilation on a real noisy sequence of sea surface temperature. The results obtained for a simple 2D velocity-vorticity formulation of Navier-Stokes (with stochastic forcing) are very promising and demonstrate the possibility to estimate a coherent velocity fields sequence from difficult images exhibiting poor photometric contrast and large regions with missing data. In future works, we plan to extend such an image based assimilation strategy to more realistic geophysical models in oceanography or meteorology.

6 Acknowledgments

The authors thank the INRIA-Microsoft joint centre, and the ANR projects PREVASSEMBLE (ANR-08-COSI-012) and Geo-Fluids (ANR-09-SYSC-005) for their financial support. They acknowledge also the Ifremer CERSAT for providing them the oceanic SST image sequence.

REFERENCES

Adrian, R., 1991: Particle imaging techniques for experimental fluid mechanics. *Annal Rev. Fluid Mech.*, **23**, 261–304.

Anderson, B. and J. Moore, 1979: *Optimal Filtering*. Englewood Cliffs, NJ : Prentice Hall.

Anderson, J. and S. Anderson, 1999: A Monte Carlo implementation of the nonlinear filtering problem to produce ensemble assimilations and forecasts. *Monthly Weather Review*, **127**(12), 2741–2758.

Bishop, C., B. Etherton, and S. Majumdar, 2001: Adaptive sampling with the ensemble transform Kalman filter. part I: Theoretical aspects. *Monthly weather review*, **129**(3), 420–436.

Bocquet, M., C. Pires, and L. Wu, 2010: Beyond gaussian statistical modeling in geophysical data assimilation. *Monthly Weather Review*, **138**, 2997–3023.

Corpetti, T., P. Héas, E. Mémin, and N. Papadakis, 2009: Pressure image asimilation for atmospheric motion estimation. *Tellus*, **61A**, 160–178.

Corpetti, T. and E. Mémin, 2012: Stochastic uncertainty models for the luminance consistency assumption. *IEEE Trans. Image Processing*, **21**(2), 481–493.

Del Moral, P., 2004: *Feynman-Kac Formulae Genealogical and Interacting Particle Systems with Applications*. Springer, New York; Series: Probability and Applications.

Doucet, A., S. Godsill, and C. Andrieu, 2000: On sequential Monte Carlo sampling methods for Bayesian filtering. *Statistics and Computing*, **10**(3), 197–208.

Elliot, F., D. Horntrop, and A. Majda, 1997: A Fourier-wavelet Monte Carlo method for fractal random fields. *Journal of Computational Physics*, **132**(2), 384–408.

Emery, W., A. Thomas, M. Collins, W. Crawford, and D. Mackas, 1986: An objective method for computing advective surface velocities from sequential infrared satellite images. *J. Geophys. Res.*, **91**, 12865–12878.

Evensen, G., 1994: Sequential data assimilation with a non linear quasi-geostrophic model using Monte Carlo methods to forecast error statistics. *J. Geophys. Res.*, **99 (C5)**(10), 143–162.

Evensen, G., 2003: The ensemble Kalman filter, theoretical formulation and practical implementation. *Ocean Dynamics*, **53**(4), 343–367.

Gordon, N., D. Salmond, and A. Smith, 1993: Novel approach to non-linear/non-gaussian bayesian state estimation. *IEEE Processing-F*, **140**(2).

Heitz, D., E. Memin, and C. Schnoerr, 2010: Variational fluid flow measurements from image sequences: synopsis and perspectives. *Exp. in Fluids*, **48**(3), 369–393.

Houtekamer, P. and H. Mitchell, 2001: A sequential ensemble Kalman filter for atmospheric data assimilation. *Monthly Weather Review*, **129**(1), 123–137.

Houtekamer, P. L. and H. Mitchell, 1998: Data assimilation using an ensemble Kalman filter technique. *Monthly Weather Review*, **126**(3), 796–811.

Hunt, B., E. Kostelich, and I. Szunyogh, 2007: Efficient data assimilation for spatiotemporal chaos: A local ensemble transform Kalman filter. *Physica D*, **230**, 112–126.

Jullien, M.-C., P. Castiglione, and P. Tabeling, 2000: Experimental observation of batchelor dispersion of passive tracers. *Phys. Rev. Lett.*, **85**, 3636–3639.

Kalman, R., 1960: A new approach to linear filtering and prediction problems. *Transactions of the ASME - Journal of Basic Engineering*, **82**, 35–45.

Kloeden, P. and E. Platen, 1999: *Numerical Solution of Stochastic Differential Equations*. Springer, Berlin.

Kraichnan, R., 1968: Small-scale structure of a randomly advected passive scalar. *Phys. Rev. Lett.* 945–963.

Lauritzen, S., 1996: *Graphical models*. Oxford University Press, Oxford,UK.

Le Dimet, F.-X., I. Navon, and D. Daescu, 2002: Second-order information in data assimilation. *Monthly Weather Review*, **130**(3), 629–648.

Lucas, B. and T. Kanade, 1981: An iterative image registration technique with an application to stereovision. In *Int. Joint Conf. on Artificial Intel. (IJCAI)*, 674–679.

Majda, A. and P. Kramer, 1999: Simplified models for turbulent diffusion:theory, numerical modelling, and physical phenomena. *Physics report*, **314**, 237–574.

Ott, E., B. Hunt, I. Szunyogh, A. Zimin, M. C. E.J. Kostelich, E. Kalnay, D. Patil, and J. A. Yorke, 2004: A local ensemble Kalman filter for atmospheric data assimilation. *Tellus*, **56A**, 415–428.

Ottenbacher, A., M. Tomasini, K. Holmund, and J. Schmetz, 1997: Low-level cloud motion winds from Meteosat high-resolution visible imagery. *Weather and Forecasting*, **12**(1), 175–184.

Papadakis, N. and E. Mémin, 2008: An optimal control technique for fluid motion estimation. *SIAM Journal on Imaging Sciences*, **1**(4), 343–363.

Papadakis, N., E. Mémin, A. Cuzol, and N. Gengembre, 2010: Data assimilation with the weighted ensemble kalman filter. *Tellus-A*, **62**(5), 673–697.

Sakov, P. and P. Oke, 2007: Implications of the form of the ensemble transformation in the ensemble square root filter. *Monthly Weather Review*, **136**, 1042–1053.

Shu, C.-W., 1998: *Advanced Numerical Approximation of Nonlinear Hyperbolic Equations*, volume 1697 of *Lecture Notes in Mathematics*. Springer Berlin / Heidelberg, 325–432.

Snyder, C., T. Bengtsson, P. Bickel, and J. Anderson, 2008: Obstacles to high-dimensional particle filtering. *Monthly Weather Review*, **136**(12), 4629–4640.

Souopgui, I., F.-X. L. Dimet, and A. Vidard, 2009: Vector field regularization by generalized diffusion. Technical Report 6844, INRIA.

Szantai, A., M. Desbois, and F. Désalmand, 2002: A method for the construction of cloud trajectories from series of satellite images. *International Journ. on. Remote Sensing*, **23**(8), 1699–1732.

Thomas, C., T. Corpetti, and E. Mémin, 2010: Data assimilation for convective cells tracking on meteorological image sequences. *IEEE trans. on Geoscience and Remote sensing*, **48**(8), 3162–3177.

Tippett, M., J. Anderson, C. B. Craig, T. Hamill, and J. Whitaker, 2003: Ensemble square root filters. *Monthly Weather Review*, **131**(7), 1485–1490.

Titaud, O., A. Vidard, I. Souopgui, and F.-X. L. Dimet, 2010: Assimilation of image sequences in numerical models. *Tellus A*, **62**(1), 30–47.

van Leeuwen, P. J., 2009: Particle filtering in geophysical systems. *Monthly Weather Review*, **137**.

Wang, X., C. Bishop, and S. Julier, 2004: Which is better, an ensemble of positive-negative pairs or a centered simplex ensemble? *Mon. Weather Rev.*, **132**, 1590–1605.

Yang, S.-C., E. Kalnay, and B. Hunt, 2012: Handling nonlinearity and non-Gaussianity in ensemble Kalman filter. *Monthly Weather Report*, **in press**.

LIST OF TABLES

1 Experiments on 2D turbulence. Results obtained from WEKF and ETKF are compared. For both filters the dynamics noise has a standard deviation of 0.01 and the parameters of the self-similar power law are fixed from the ground truth data. Mean square estimation errors with respect to the ground truth are presented on the first table, the ensemble dispersion around the ground truth is indicated on the second table. Note the ground truth is associated to a zero variance as it is a deterministic system. The mean has been computed through an empirical average over the 20 last image frames of 10 realizations

Results (mean estimation)		
Number of members	WETKF	ETKF
10	0.145	0.146
50	0.079	0.083
150	0.051	0.052
400	0.043	0.044

Results (ensemble dispersion)		
Number of members	WETKF	ETKF
10	0.146	0.147
50	0.080	0.084
150	0.053	0.053
400	0.045	0.046

Table 1. Experiments on 2D turbulence. Results obtained from WEKF and ETKF are compared. For both filters the dynamics noise has a standard deviation of 0.01 and the parameters of the self-similar power law are fixed from the ground truth data. Mean square estimation errors with respect to the ground truth are presented on the first table, the ensemble dispersion around the ground truth is indicated on the second table. Note the ground truth is associated to a zero variance as it is a deterministic system. The mean has been computed through an empirical average over the 20 last image frames of 10 realizations

LIST OF FIGURES

9 Real 2D turbulent flow (Jullien et al., 2000). (a) Image at given time k and estimated velocity field with SLK; (b) Image at given time k and estimated velocity field with WEnKF assimilation of SLK result; (c) Image at given time k and estimated velocity field with WETKF direct assimilation of image data; (d) Vorticity estimate with SLK and associated velocity field; (e) Mean estimate of vorticity with WEnKF assimilation of SLK observation, and associated velocity field; (f) Mean estimate of vorticity with WETKF direct assimilation of image data, and associated velocity field; (g)-(h)-(i) Zoom in on white delimited areas of (d)-(e)-(f).

10 Synthetic oceanic sequence with missing data. (a) Image at given time k; (b) Image at given time $k+1$; (c) Ground truth vorticity and velocity field; (d) Mean estimate of vorticity and velocity from WETKF assimilation of images without missing data; (e) Mean estimate of vorticity and velocity from WETKF assimilation of images with missing data shown in (a)-(b).

11 Synthetic oceanic sequence with missing data. (a) RMSE between mean estimate of vorticity and ground truth; (b) RMSE between mean estimate of velocity and ground truth.

12 Real satellite sequence of SST (sea surface temperature) images. Dark blue regions indicate missing data due to the cloud cover or land regions. First column: SST images at different times $k = 1, 10, 24, 39, 49$ and estimated velocity fields with the WETKF assimilation of image data; Second column: Mean estimated vorticity with WETKF and associated velocity fields.

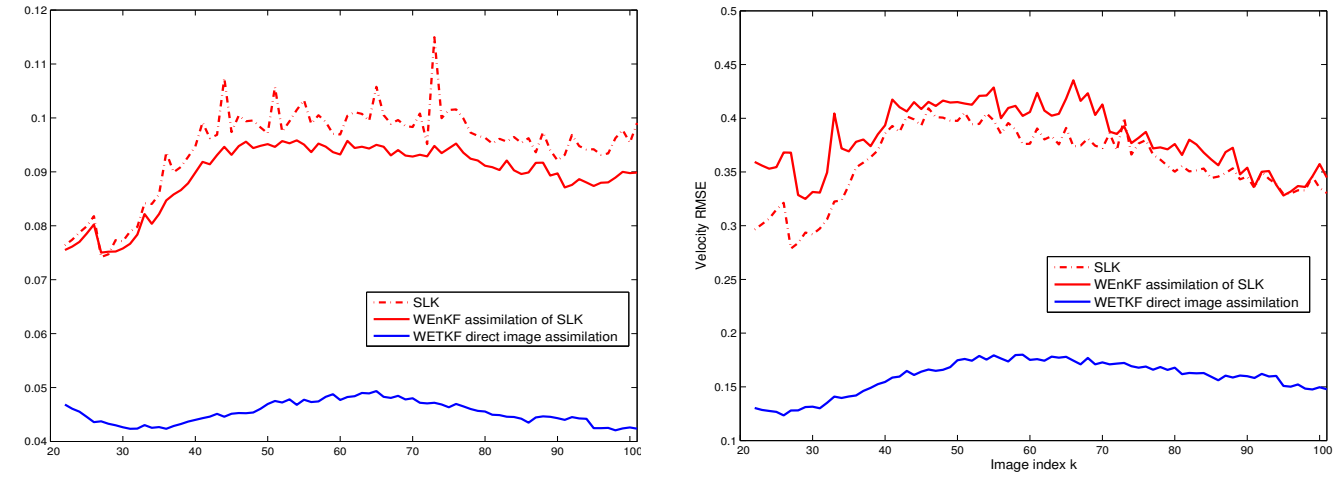

(a) (b)

Figure 1. Synthetic 2D turbulent flow. (a) RMSE between mean estimate of vorticity and ground truth; (b) RMSE between mean estimate of velocity and ground truth.

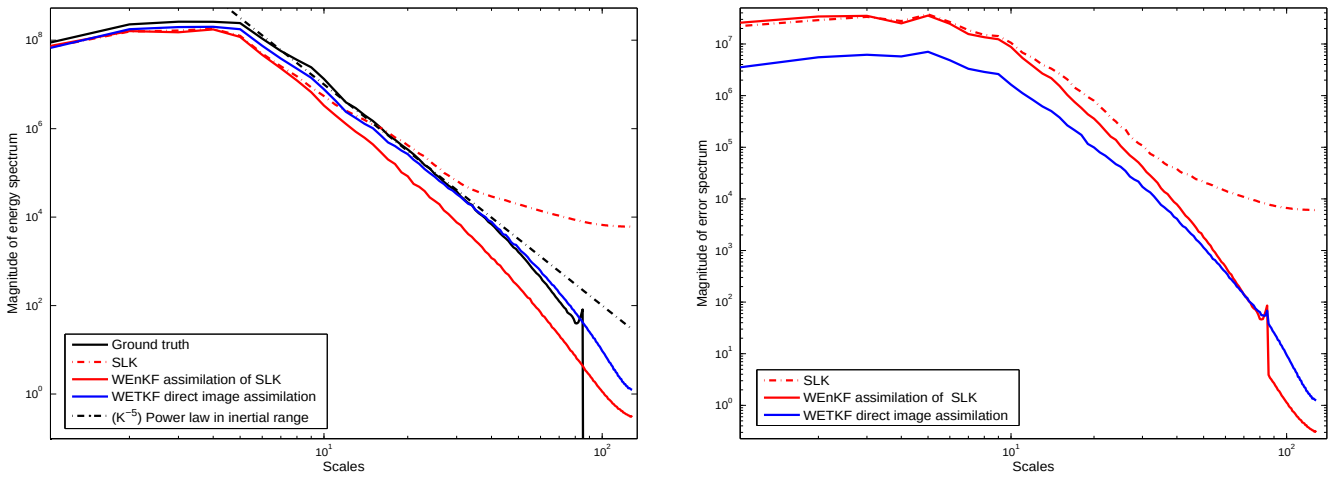

(a) (b)

Figure 2. Synthetic 2D turbulent flow. (a) Energy spectra; (b) Error energy spectra.

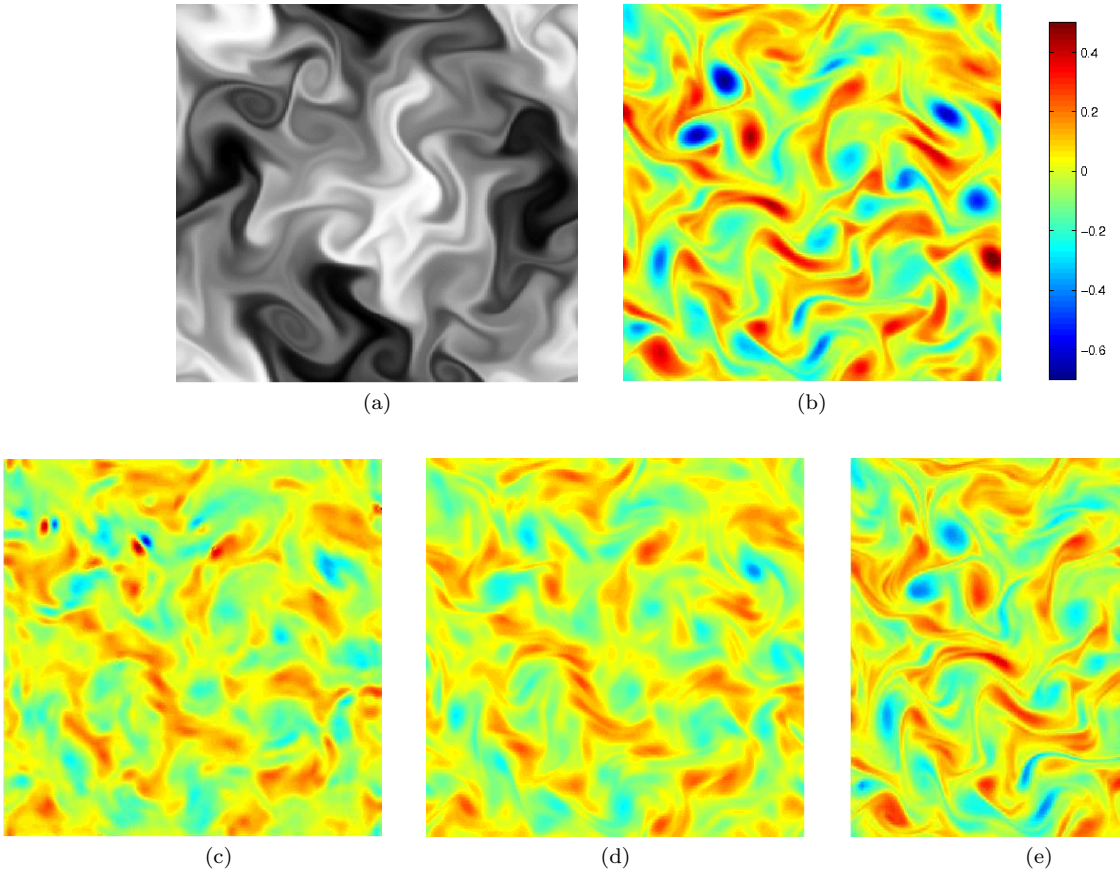

Figure 3. Synthetic 2D turbulent flow. (a) Example of scalar image of the sequence at given time k; (b) Ground truth vorticity at time k; (c) SLK vorticity estimate; (c) Mean estimate of vorticity with WEnKF assimilation of SLK observation; (d) Mean estimate of vorticity with WETKF direct assimilation of image data.

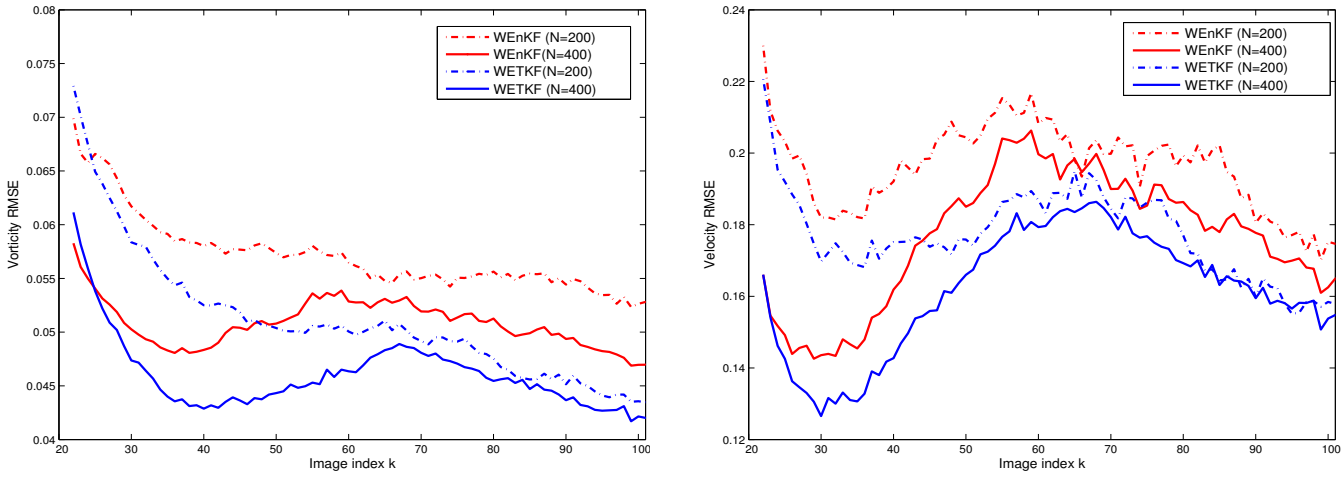

Figure 4. Comparison of WEnKF and WETKF techniques for the direct assimilation of image data. (a) RMSE between mean estimate of vorticity and ground truth; (b) RMSE between mean estimate of velocity and ground truth.

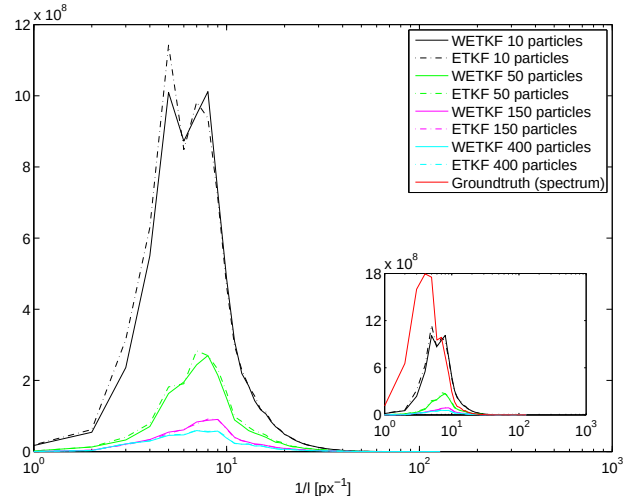

(a) Error energy spectrum $\log(k) \times k\widehat{E}_{Err}(k)$

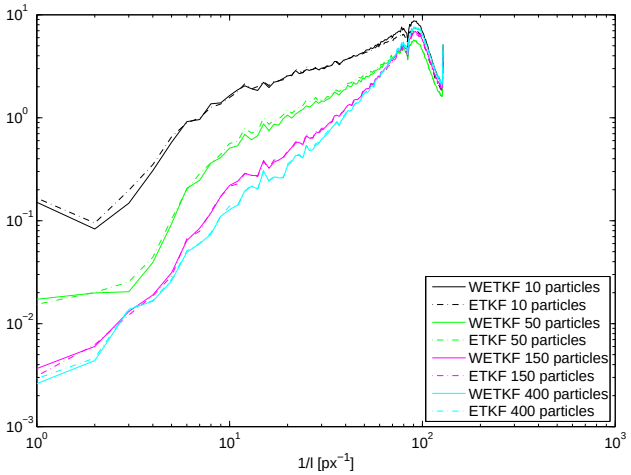

(b) Normalized error energy spectrum $\log(k) \times \log(\widehat{E}_{Err}(k))/(\log \widehat{E}_{ref}(k))$

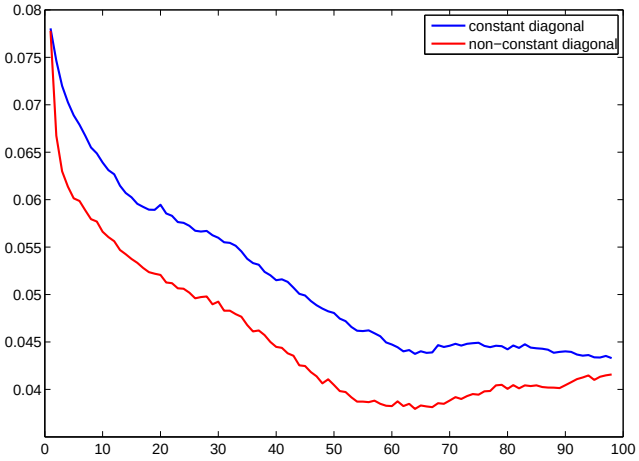

(c) image frame *vs* vorticity RMSE

Figure 5. (a) Error Energy spectrum in $\log k$ *vs.* $kE(k)$ scale obtained with ETKF (dotted lines) and WETKF (plain lines) for different number of particles; (b) Energy spectrum in log-log scale obtained with ETKF (dotted lines) and WETKF (plain lines) for different number of particles; (c) vorticity root-mean-square error along time obtained for WETKF with a diagonal constant observation variance (blue) and with the empirical image based variance (red).

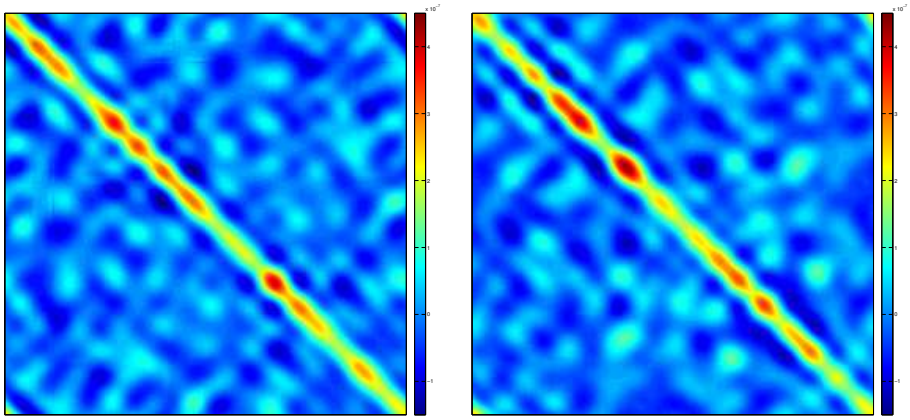

Figure 6. Visualization(with 50 members) of the covariance matrix values corresponding to the central line at $t = 99$ left: ETKF, right: WETKF . The significative covariance length-scale is about $15 \times \Delta x$ large for both filters

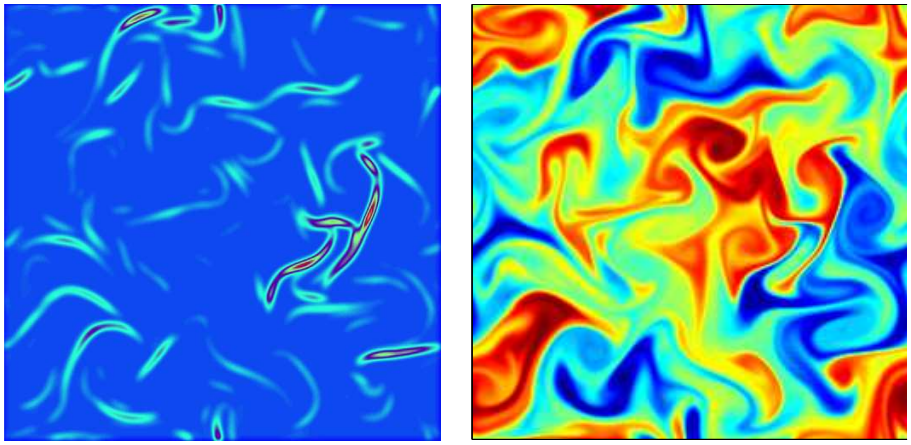

Figure 7. Left: visualization for WETKF (with 400 members) of an example of the image based adapted variance map associated to the displaced frame observation model ; Right: corresponding image of the passive scalar. High values of the standard deviation correspond to areas associated with high photometric gradient

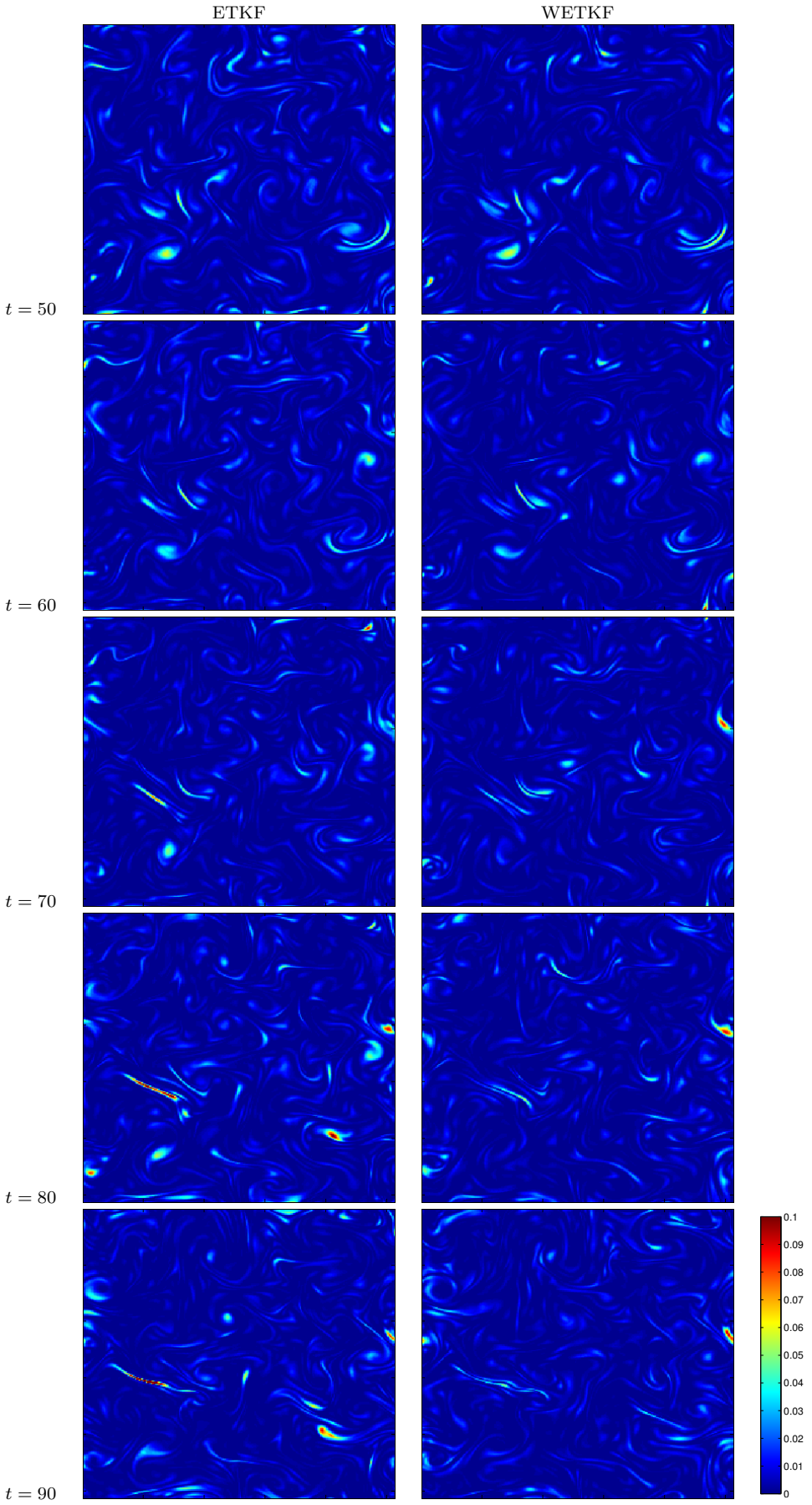

Figure 8. Example of the ensemble dispersion maps evolution along time; left column ETKF ensemble dispersion; right column WETKF ensemble dispersion

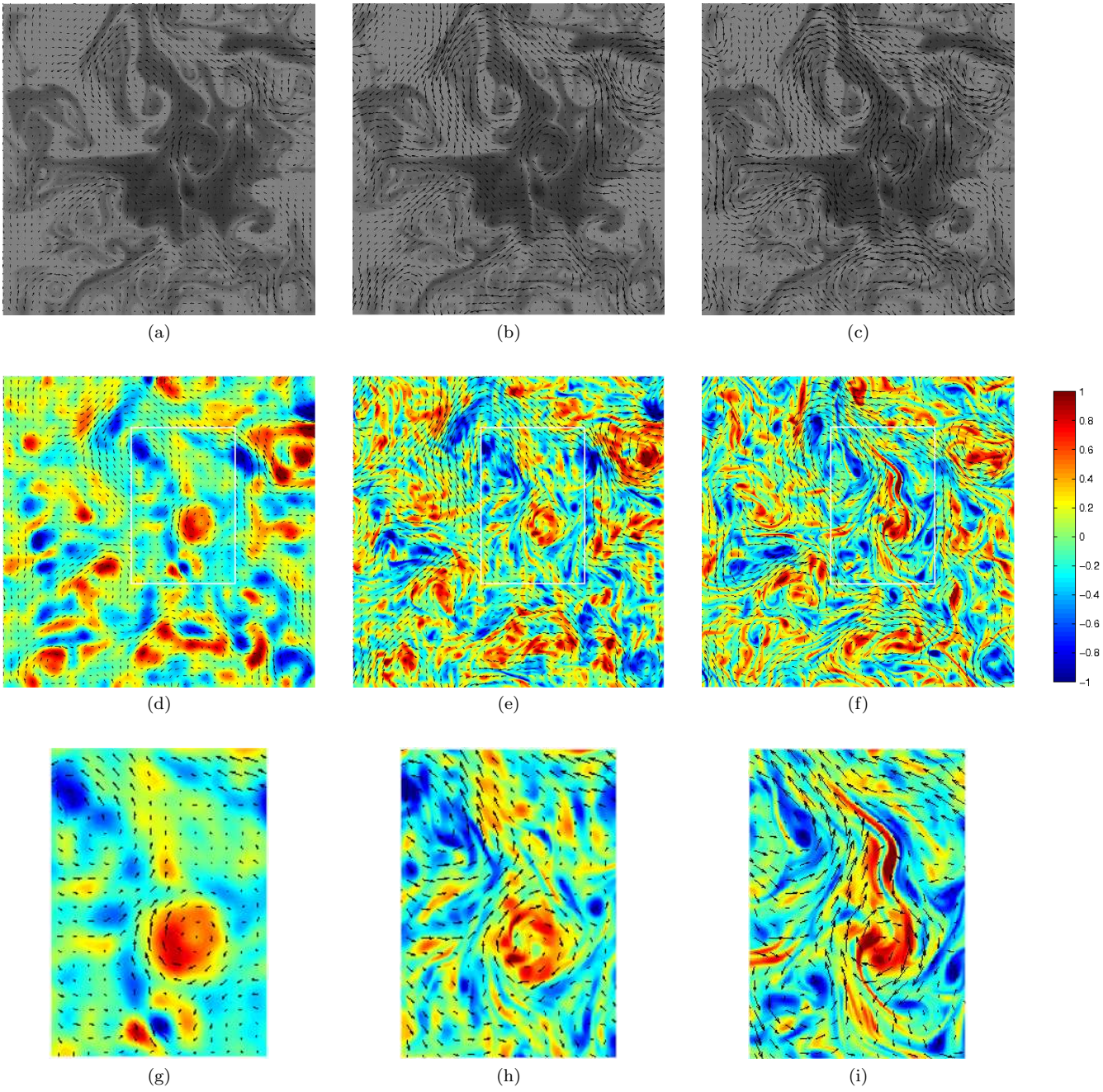

Figure 9. Real 2D turbulent flow (Jullien et al., 2000). (a) Image at given time k and estimated velocity field with SLK; (b) Image at given time k and estimated velocity field with WEnKF assimilation of SLK result; (c) Image at given time k and estimated velocity field with WETKF direct assimilation of image data; (d) Vorticity estimate with SLK and associated velocity field; (e) Mean estimate of vorticity with WEnKF assimilation of SLK observation, and associated velocity field; (f) Mean estimate of vorticity with WETKF direct assimilation of image data, and associated velocity field; (g)-(h)-(i) Zoom in on white delimited areas of (d)-(e)-(f).

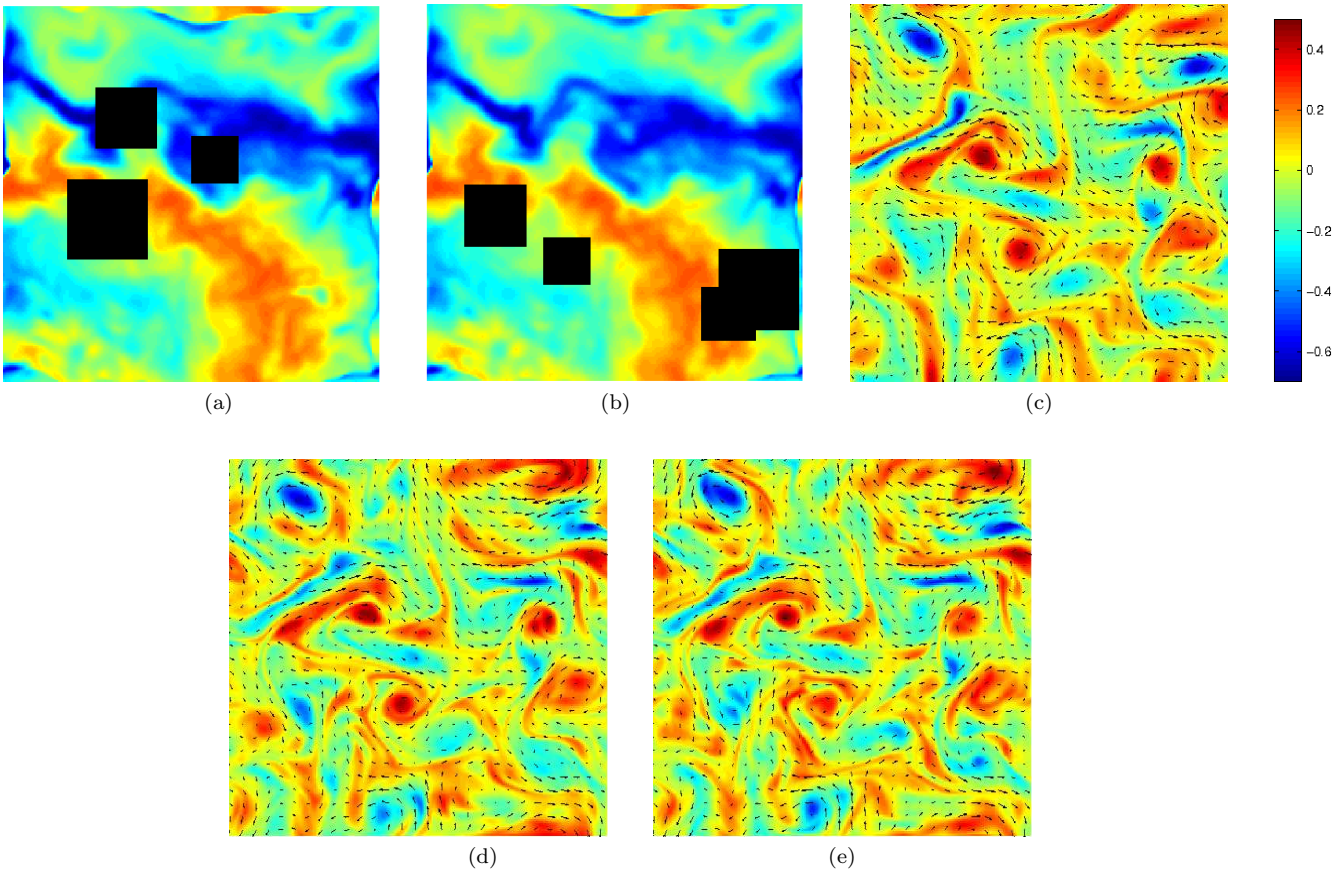

Figure 10. Synthetic oceanic sequence with missing data. (a) Image at given time k; (b) Image at given time $k+1$; (c) Ground truth vorticity and velocity field; (d) Mean estimate of vorticity and velocity from WETKF assimilation of images without missing data; (e) Mean estimate of vorticity and velocity from WETKF assimilation of images with missing data shown in (a)-(b).

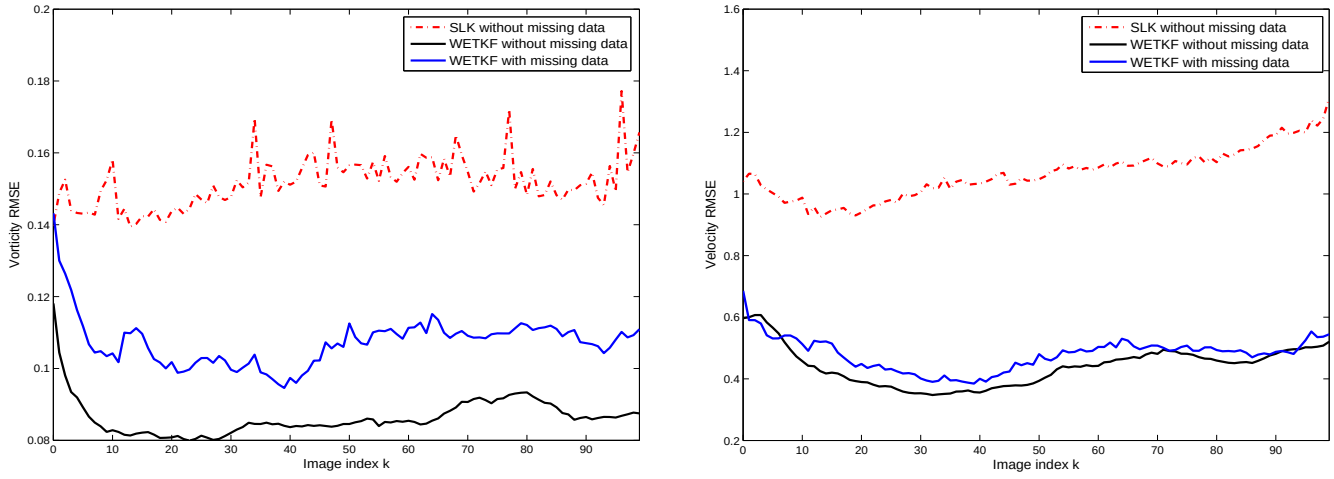

Figure 11. Synthetic oceanic sequence with missing data. (a) RMSE between mean estimate of vorticity and ground truth; (b) RMSE between mean estimate of velocity and ground truth.

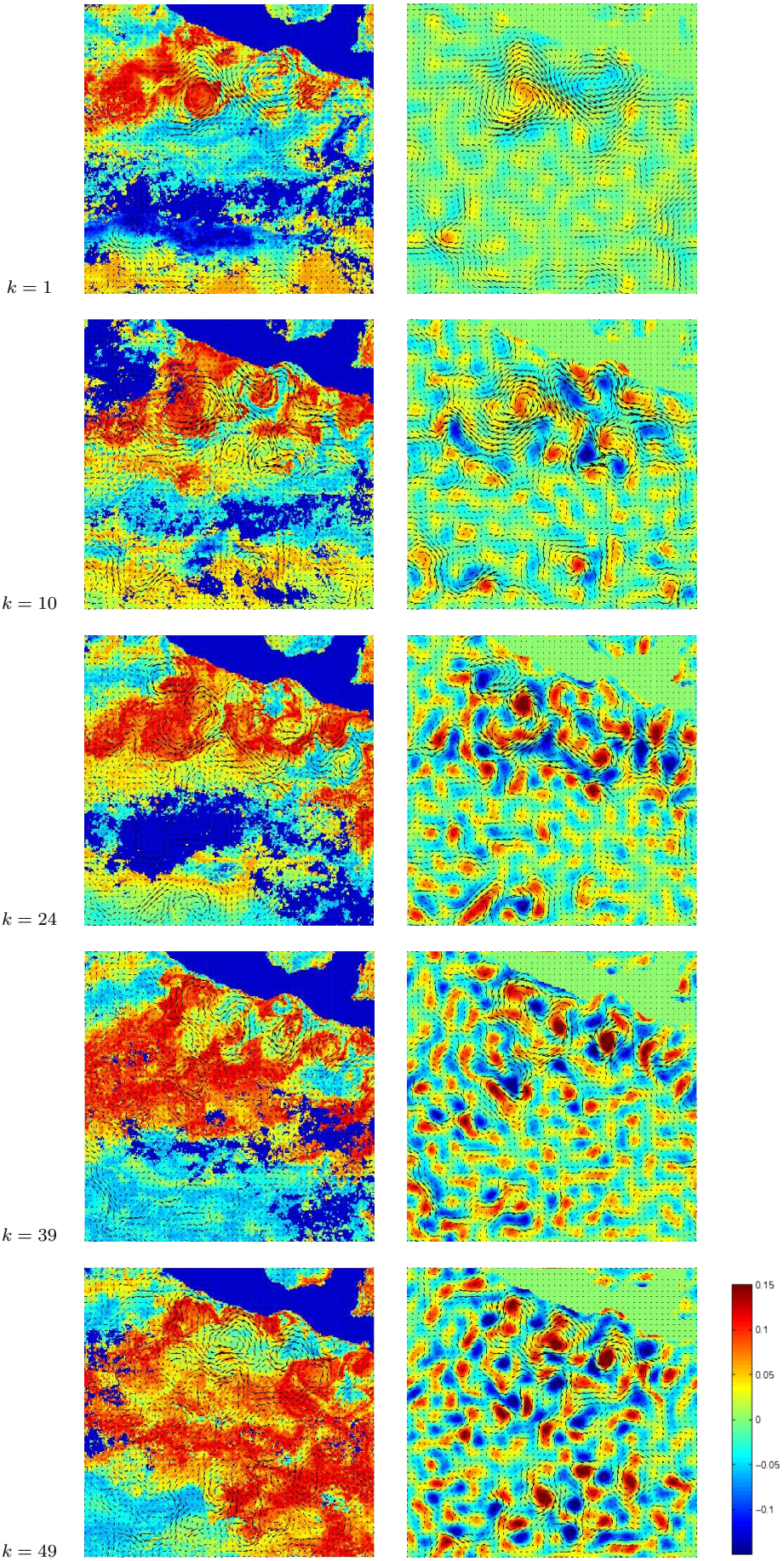

Figure 12. Real satellite sequence of SST (sea surface temperature) images. Dark blue regions indicate missing data due to the cloud cover or land regions. First column: SST images at different times $k = 1, 10, 24, 39, 49$ and estimated velocity fields with the WETKF assimilation of image data; Second column: Mean estimated vorticity with WETKF and associated velocity fields.